Concurrence of quantum anomalous Hall and topological Hall effects in magnetic topological insulator sandwich heterostructures

Jue Jiang^{1,4}, Di Xiao ^{1,4}, Fei Wang¹, Jae-Ho Shin¹, Domenico Andreoli², Jianxiao Zhang¹, Run Xiao¹, Yi-Fan Zhao¹, Morteza Kayyalha¹, Ling Zhang¹, Ke Wang³, Jiadong Zang², Chaoxing Liu¹, Nitin Samarth ^{1,4}, Moses H. W. Chan ^{1,4} and Cui-Zu Chang ^{1,4}

The quantum anomalous Hall (QAH) effect is a consequence of non-zero Berry curvature in momentum space. The QAH insulator harbours dissipation-free chiral edge states in the absence of an external magnetic field. However, the topological Hall (TH) effect, a hallmark of chiral spin textures, is a consequence of real-space Berry curvature. Here, by inserting a topological insulator (TI) layer between two magnetic TI layers, we realized the concurrence of the TH effect and the QAH effect through electric-field gating. The TH effect is probed by bulk carriers, whereas the QAH effect is characterized by chiral edge states. The appearance of the TH effect in the QAH insulating regime is a consequence of chiral magnetic domain walls that result from the gate-induced Dzyaloshinskii-Moriya interaction and occurs during the magnetization reversal process in the magnetic TI sandwich samples. The coexistence of chiral edge states and chiral spin textures provides a platform for proof-of-concept dissipationless spin-textured spintronic applications.

lectronic band structures of non-trivial topology in momentum space and magnetic chiral spin textures in real space have attracted enormous attention in the past decade as they harbour elegant Berry curvature physics¹⁻³. The intrinsic anomalous Hall (AH) effect is such an example: it is induced by the Berry curvature in momentum space in ferromagnetic (FM) materials⁴ and can even be quantized under certain circumstances, which leads to the quantum anomalous Hall (QAH) effect. The QAH effect has been theoretically proposed⁵⁻⁸ and experimentally realized⁹⁻¹³ in magnetically doped topological insulator (TI) films. However, chiral spin textures (for example, skyrmions) provide another example of non-trivial topology, but in real space. It has been shown that chiral spin textures can also induce a Hall current—this is known as the topological Hall (TH) effect and is generally regarded as the transport signature of non-zero spin chirality³. The TH effect has been experimentally observed in many metallic systems, such as MnSi (refs. 14,15), MnGe (ref. 16), FeGe (ref. 17) and the SrIrO $_3$ /SrRuO $_3$ interface 18,19 , as well as magnetically doped TI films and heterostructures^{20,21}.

The QAH and TH effects have been separately observed in magnetically doped TI^{9,10,20,21}, with distinctly different sample geometries. The QAH effect can be realized only in the insulating regime of a magnetic TI⁹⁻¹³, whereas the TH effect is usually seen in metallic systems^{20,21}. In this article, we realize the TH effect in the insulating regime of magnetic TI and demonstrate the concurrence of the QAH and TH effects in a single sample. This concurrence provides a new platform to understand the interplay between the chiral edge states of the QAH effect and the chiral spin textures associated with the TH effect.

To realize the QAH and TH effects in one TI-based device, the sample needs to accommodate three conditions: (1) the time-reversal symmetry is broken, which is the common prerequisite for both QAH and TH effects, (2) the chemical potentials of the top and bottom surfaces can be simultaneously tuned near the magnetization exchange gaps, which is essential for the QAH effect and (3) A significant Dzyaloshinskii–Moriya (DM) interaction, $H = D_{ii}(S_i \times S_i)$, can be created, which is required for the TH effect. Here D_{ii} stands for the magnitude and orientation of the DM interaction and S. and S_i are two neighbouring spins. Recently, two papers reported the observation of the TH effect in TI. One is about Cr-(Bi,Sb)₂Te₃/ (Bi,Sb)₂Te₃ bilayer structures, in which only one surface is gapped owing to the magnetic exchange interaction²⁰. The consequential spatial asymmetry thus favours the formation of the DM interaction and gives rise to the TH effect in this bilayer structure when it is tuned into the p-type metallic regime. However, the QAH effect cannot be realized in such a bilayer sample geometry as the other surface is non-magnetic and gapless. The other paper is about four quintuple layers (QL) Mn-doped Bi₂Te₃ films without a Te capping layer on a SrTiO₃ substrate, in which the TH effect was observed in both p- and n-type metallic regimes²¹. As the Dirac point is buried under the bulk valence bands in Bi, Te, films^{22,23}, the QAH state is also unlikely in Mn-doped Bi₂Te₃ samples. In uniformly doped QAH samples, the inversion symmetry is preserved in the bulk^{9,10}, so that the DM interaction is induced only on the top and bottom surfaces^{24,25}. However, the DM interactions from the two opposite surface states (SSs) have opposite signs. When the two surfaces are strongly coupled, spin chirality cannot be achieved. Effectively, the overall DM interaction felt by the magnetization is greatly reduced and it is difficult to realize the TH effect in such uniformly doped QAH samples. Therefore, to realize the concurrence of the QAH and TH effects in a single sample, the two surfaces of a QAH sample should be separated and inversion symmetry must be broken to induce a finite DM interaction.

¹Department of Physics, The Pennsylvania State University, University Park, PA, USA. ²Department of Physics, University of New Hampshire, Durham, NH, USA. ³Materials Research Institute, The Pennsylvania State University, University Park, PA, USA. ⁴These authors contributed equally: Jue Jiang, Di Xiao. *e-mail: nxs16@psu.edu; mhc2@psu.edu; cxc955@psu.edu

NATURE MATERIALS ARTICLES

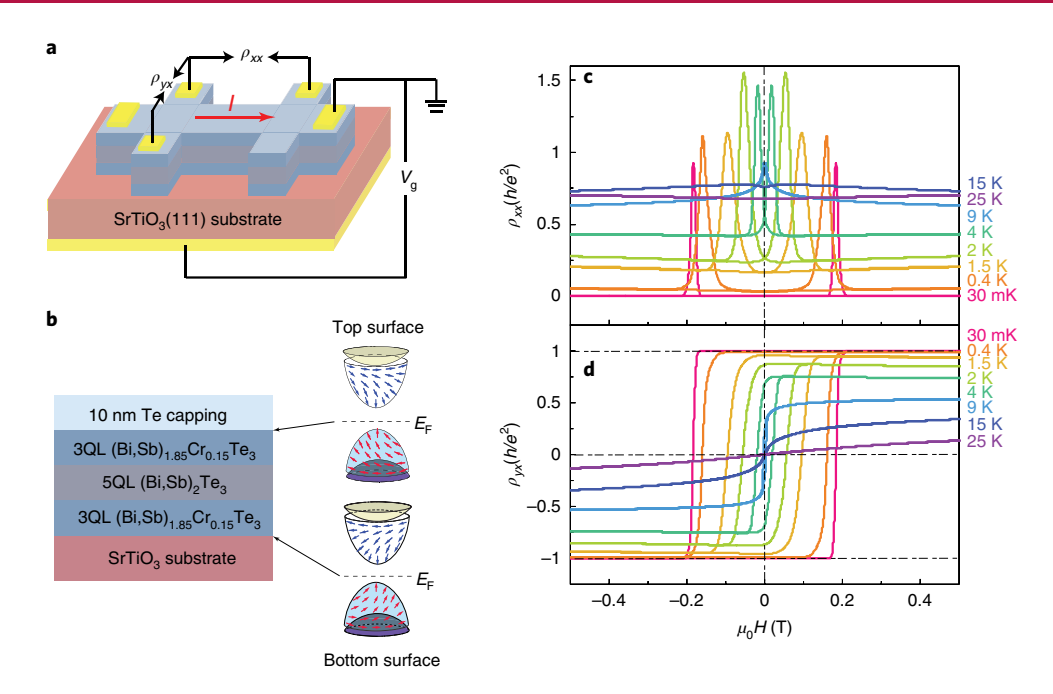


Fig. 1 | QAH effect in TI sandwich heterostructures. a, Schematic of the field-effect transistor device with a bottom gate (V_g) used in transport measurements. The electrical contacts on the Hall bar and the back-gate contact shown in yellow are made by pressed indium dots. The 0.5 mm SrTiO₃(111) substrate is used as the dielectric layer for the bottom gate. **b**, Schematic of the magnetic TI sandwich heterostructure. The total thickness of the sample is 11 QLs. When $T < T_c$, an exchange gap opens at the Dirac points of the top and bottom surfaces. Blue (red) arrows represent the spin orientations of the top (bottom) section of gapped Dirac SSs. **c,d**, Magnetic field $\mu_0 H$ dependence of the longitudinal resistance ρ_{xx} (**c**) and the Hall resistance ρ_{yx} (**d**) at $V_g = 0$ V. At T = 30 mK and $V_g = 0$ V, the quantized ρ_{yx} and the vanishing ρ_{xx} suggest this sandwich sample is in the QAH state.

Molecular beam epitaxy growth and magnetotransport of the 3-5-3 magnetic TI heterostructure

We fabricated a TI-based sandwich structure with an undoped TI layer (5 quintuple (Bi,Sb)₂Te₃ layers) inserted between two magnetic TI layers (two 3 quintuple Cr-doped (Bi,Sb),Te, layers) (Fig. 1a,b). Such a 3-5-3 sandwich heterostructure has two distinct advantages. First, the non-magnetic TI layer serves as a spacer that separates the magnetic exchange interaction between the two magnetic TI layers²⁶⁻²⁸. As a result, the influence of the DM interaction can be maximized because the magnetic moments in each magnetic TI layer interact only with their own SSs. Second, both the top and bottom SSs are separately gapped by the magnetization, which thus makes the QAH effect possible. We performed the electrical transport measurements on the 3-5-3 heterostructure with standard Hall bar geometry. When the bottom gate $V_g = 0 \text{ V}$, the FM order at low temperatures gaps out the top and bottom SSs, and the chemical potential is located inside the magnetic exchange gaps of both surfaces (Fig. 1b). This is confirmed by the observation of a perfectly quantized Hall resistance (ρ_{yx}) and a vanishing longitudinal resistance (ρ_{xx}) at $T = 30 \,\text{mK}$ (Fig. 1c,d). With increasing temperature, the sample deviates from the QAH state and shows transport properties of a conventional FM material, namely, hysteretic ρ_{vx} loops and butterfly-shaped ρ_{xx} . The Curie temperature (T_C) of the 3-5-3 sandwich heterostructure sample is determined to be ~19K by means of Arrott plots (Supplementary Fig. 4).

Gate-induced TH 'hump' feature in the 3-5-3 magnetic TI heterostructure

Figure 2 shows the magnetic-field μ_0H dependence of the Hall resistance ρ_{yx} and the longitudinal resistance ρ_{xx} of the 3-5-3 heterostructure at different gate voltages $(V_{\rm g}-V_{\rm g}^0)$. When $V_{\rm g}=V_{\rm g}^0=+20\,{\rm V}$, the sample displays a perfect QAH state: at zero magnetic field, $\rho_{yx}(0)=\pm h/e^2$ and $\rho_{xx}(0)<1\,\Omega$. When the magnetic field $\mu_0H>\mu_0H_c$ (μ_0H_c is the coercive field), the Hall curves completely overlap

during the upward and downward magnetic field sweeps (Fig. 2d). When $V_g - V_g^0 = -100 \,\text{V}$, hole carriers are injected into the sample and dissipative bulk channels are introduced. In this regime, $\rho_{vx}(0)$ deviates from h/e^2 but still remains as high as $\sim 0.76 \, h/e^2$ and $\rho_{vx}(0)/\rho_{xx}(0) \approx 1.2$, which indicates the persistence of the chiral edge transport of the QAH state9. The existence of chiral edge transport is further supported by the decrease in $\rho_{xx}(0)$ with decreasing temperature (Fig. 3e), which we discuss in detail below. Notably, over a range of a fraction of a Tesla above $\mu_0 H_c$, a hump feature appears in the ρ_{vx} curves (green shadow area); specifically, the Hall curve under a downward μ_0H sweep does not overlap with that under an upward $\mu_0 H$ sweep when $\mu_0 H > \mu_0 H_c$ (Fig. 2c). The hump feature observed here has been interpreted as a signature of the TH effect and is considered as strong evidence for the existence of chiral spin textures in real space^{3,14-21}. Therefore, by adjusting the chemical potential using the bottom gate, we realized the concurrence of QAH and TH effects in the insulating regime of the magnetic TI sandwich sample. This hump feature of the TH effect becomes more pronounced when the chemical potential is further tuned towards the bulk valence bands (Fig. 2a,b).

At $V_{\rm g}-V_{\rm g}^0=+70\,{\rm V}$, electron carriers are introduced and a trace of the hump feature of TH effect also appears (Fig. 2e). The observation of $\rho_{yx}(0)\approx 0.85h/e^2$ and $\rho_{yx}(0)/\rho_{xx}(0)\approx 4.6$ demonstrates the existence of the QAH state. Therefore, the QAH effect is also concurrent with the TH effect for $V_{\rm g}-V_{\rm g}^0=+70\,{\rm V}$. When more electrons are introduced, the hump feature of the TH effect fades away (Fig. 2f). The asymmetric behaviour of the TH effect in n- and p-type regions is possibly a result of the non-symmetric electronic band structure of TI^{23,29}, which we discuss below. We note that the slope of the Hall traces at high magnetic fields $(0.5\,{\rm T}<\mu_0{\rm H}<1.5\,{\rm T})$ is always negative in both $V_{\rm g}< V_{\rm g}^0$ and $V_{\rm g}> V_{\rm g}^0$ regions, which suggests that the standard Hall coefficient $R_{\rm N}$ cannot be used to estimate carrier density near the QAH regime (Supplementary Fig. 9 and the relevant discussion).

ARTICLES NATURE MATERIALS

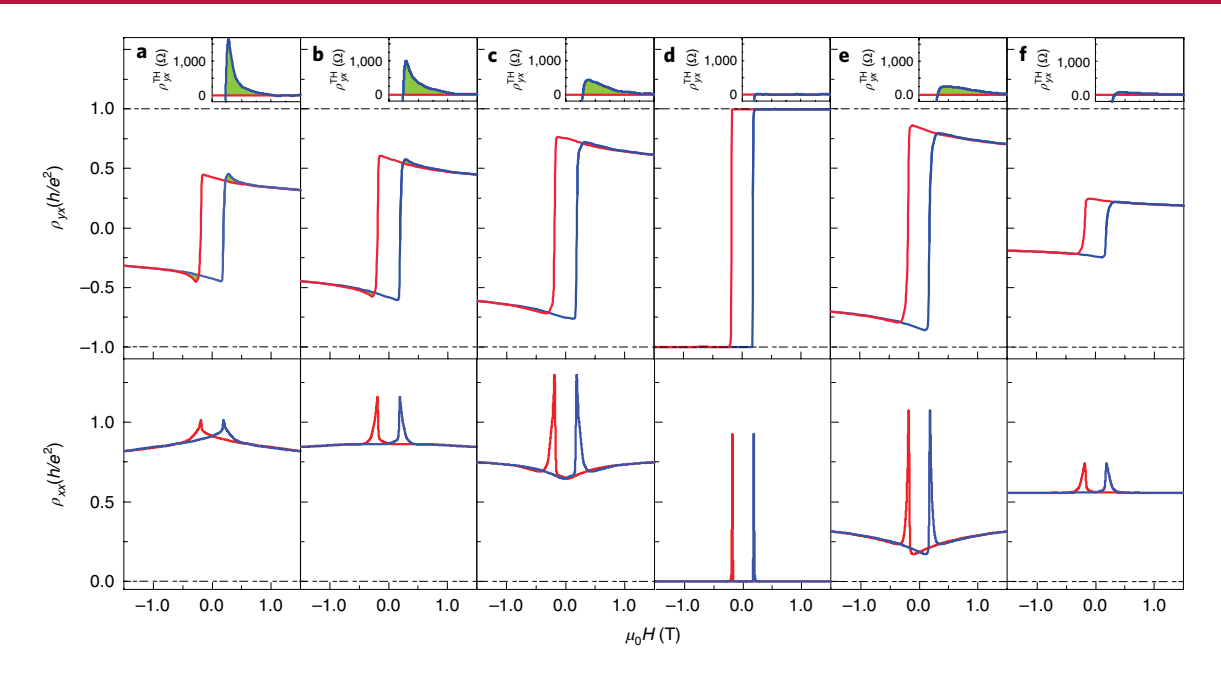


Fig. 2 | **Gate-induced TH effect in TI sandwich heterostructures. a-f**, Magnetic-field $\mu_0 H$ dependence of the Hall resistance ρ_{yx} (top) and the longitudinal resistance ρ_{xx} (bottom) at different gates ($V_g - V_g^0$) of -220 V (**a**), -140 V (**b**), -100 V (**c**), 0 V (**d**), +70 V (**e**) and +180 V (**f**) at T = 30 mK. The sample shows a perfect QAH state when $V_g = V_g^0 = +20$ V. When V_g is tuned away from V_g^0 , ρ_{yx} deviates from the quantized value (that is, \hbar/e^2) and shows a hump (feature shaded in green), which is known as the TH effect. Insets **a-f**: the TH resistance ρ_{yx}^{TH} , which is subtracted using the offset resistance of ρ_{yx} as the external $\mu_0 H$ is swept upward and downward. Blue (red) curve represents the process for increasing (decreasing) $\mu_0 H$.

In a FM material, the total ρ_{yx} is a result of three contributions: the normal Hall (NH) resistance $\rho_{yx}^{\rm NH}$, the AH resistance $\rho_{yx}^{\rm AH}$ and $\rho_{yx}^{\rm TH}$:

$$\rho_{yx} = \rho_{yx}^{\rm NH} + \rho_{yx}^{\rm AH} + \rho_{yx}^{\rm TH} \tag{1}$$

To single out the TH component $\rho_{yx}^{\rm TH}$, we need to subtract $\rho_{yx}^{\rm NH}$ and $\rho_{yx}^{\rm AH}$ from ρ_{yx} . Here we interpret the offset resistance under upward and downward μ_0 H sweeps (green shadow area in Fig. 2) as ρ_{uv}^{TH} for the following reasons. Let us consider the positive μ_0H regime. During the downward μ_0H sweep (red curves in Fig. 2), the system should be in a FM state without any chiral spin textures and thus ρ_{yx} should include ρ_{yx}^{NH} and ρ_{yx}^{AH} . For the upward $\mu_0 H$ sweep (blue curves in Fig. 2), the system undergoes a magnetic transition around $\mu_0 H_c$ and chiral spin textures, particularly chiral magnetic domain walls (Fig. 4a,b and the relevant discussion), can be formed. In this situation, all three Hall contributions are present and ρ_{vx}^{NH+} ρ_{vx}^{AH} keeps the same value during the downward $\mu_0 H$ sweep. ρ_{yx} ρ_{yx} seeps the same value during the downward μ_{0} 11 sweep. Thus, $\rho_{yx}^{\rm TH}$ can be extracted by the difference between the red and blue curves²¹. We emphasize that the standard expressions for $\rho_{yx}^{\rm NH}$ and $\rho_{yx}^{\rm AH}$ ($\rho_{yx}^{\rm NH} = \mu_0 R_{\rm N} H$ and $\rho_{yx}^{\rm AH} = R_{\rm A} M$ with the AH coefficient $R_{\rm A}$ and the sample magnetization M (refs. ^{9,30,31})) are applicable only for metallic systems and thus not valid for our samples close to the QAH insulating regime (Supplementary Fig. 9 and the relevant discussion). When $V_g - V_g^0 = -220 \text{ V}$, the maximum of ρ_{yx}^{TH} is ~1.65 k Ω , which is much larger than the TH resistances observed in all previous studies on metallic systems^{3,14-21}.

Concurrence of QAH and TH effects

To locate the region for the coexistence of the QAH and TH effects, we summarize the $V_{\rm g}-V_{\rm g}^0$ dependence of $\rho_{\rm yx}(0)$, $\rho_{\rm xx}(0)$ and $\rho_{\rm yx}^{\rm TH}$ at $T=30\,{\rm mK}$ (Fig. 3a,b). When $-30\,{\rm V} \le V_{\rm g}-V_{\rm g}^0 \le +40\,{\rm V}$, the sample exhibits a perfect QAH state, that is $\rho_{\rm yx}(0)$ is fully quantized, and $\rho_{\rm xx}(0)$ and $\rho_{\rm yx}^{\rm TH}$ are vanishingly small. The perfect QAH state is further validated by the temperature dependence of $\rho_{\rm xx}(0)$ and $\rho_{\rm yx}(0)$ (Fig. 3f). When $V_{\rm g}-V_{\rm g}^0$ is tuned from $-30\,{\rm V}$ to $-140\,{\rm V}$, the sample

shows the non-perfect QAH state, in which the current flows through both the dissipationless chiral edge channels and the dissipative bulk channels 32 . $\rho_{yx}(0)$ decreases from $\sim h/e^2$ to $\sim 0.59 h/e^2$, whereas $\rho_{xx}(0)$ increases from ~ 0 to $\sim 0.87 h/e^2$. As noted above, the existence of the QAH state for $V_{\rm g} - V_{\rm g}^0 = -100\,{\rm V}$ and $-140\,{\rm V}$ can be further confirmed by the decrease in $\rho_{xx}(0)$ and the increase in $\rho_{yx}(0)$ with decreasing temperature (Fig. 3d,e). The contrasting temperature dependences of $\rho_{xx}(0)$ and $\rho_{yx}(0)$, together with the large $\rho_{yx}(0)/\rho_{xx}(0)$ ratio, can only be a result of the chiral edge states, which thus provides conclusive evidence for the existence of the QAH state. Simultaneously, $\rho_{yx}^{\rm TH}$ increases monotonically between $-140\,{\rm V}$ and $-30\,{\rm V}$ for $V_{\rm g} - V_{\rm g}^0$, which demonstrates the presence of the TH effect as well as the QAH effect. In other words, the chiral spin textures coexist with chiral edge states. When $V_{\rm g} - V_{\rm g}^0$ is further tuned from $-140\,{\rm V}$ to $-220\,{\rm V}$, the signature of the QAH state disappears; with $\rho_{xx}(0)$ and $\rho_{yx}(0)$ showing a similar temperature dependence (Fig. 3c), only the TH effect is seen in this regime.

The QAH state persists for $(V_g - V_g^0)$ greater than +40 V up to +100 V with $\rho_{yx}(0) \approx 0.49 h/e^2$ and $\rho_{yx}(0)/\rho_{xx}(0) \approx 1.1$. The presence of the QAH state at $V_g - V_g^0 = +70$ V is also verified by the decrease in $\rho_{xx}(0)$ and the increase in $\rho_{yx}(0)$ with decreasing temperature (Fig. 3g). In this regime, a smaller ρ_{yx}^{TH} as compared to that in the p-doped regime (that is, $V_g < V_g^0$) is found. Therefore, for +40 V < $V_g - V_g^0 \le +100$ V, the TH effect is also concurrent with the QAH effect. When $V_g - V_g^0$ is further increased from +100 V to +180 V, the similar temperature dependence of $\rho_{xx}(0)$ and $\rho_{yx}(0)$ marks the disappearance of the QAH state (Fig. 3h), and only the TH effect is seen. The much smaller ρ_{yx}^{TH} for $V_g > V_g^0$ indicates that the chemical potential of the system has not crossed the bulk conduction bands. As we discuss in detail below, this implies that the TH feature at $V_g > V_g^0$ is solely induced by the asymmetric potential between the top and bottom surfaces crossing the helical SSs³2,3³.

TH feature at $V_g > V_g^0$ is solely induced by the asymmetric potential between the top and bottom surfaces crossing the helical SSs^{32,33}. Figure 3i shows the $\mu_0 H$ dependence of $\rho_{yx}^{\rm TH}$ with the maximum peak at different temperatures under $V_g = V_g^{\rm TH,max}$. $\rho_{yx}^{\rm TH}$ decreases gradually with temperature from 30 mK and disappears at T=5 K. The peak position of $\rho_{yx}^{\rm TH}$ and the magnetic field range of the hump

NATURE MATERIALS ARTICLES

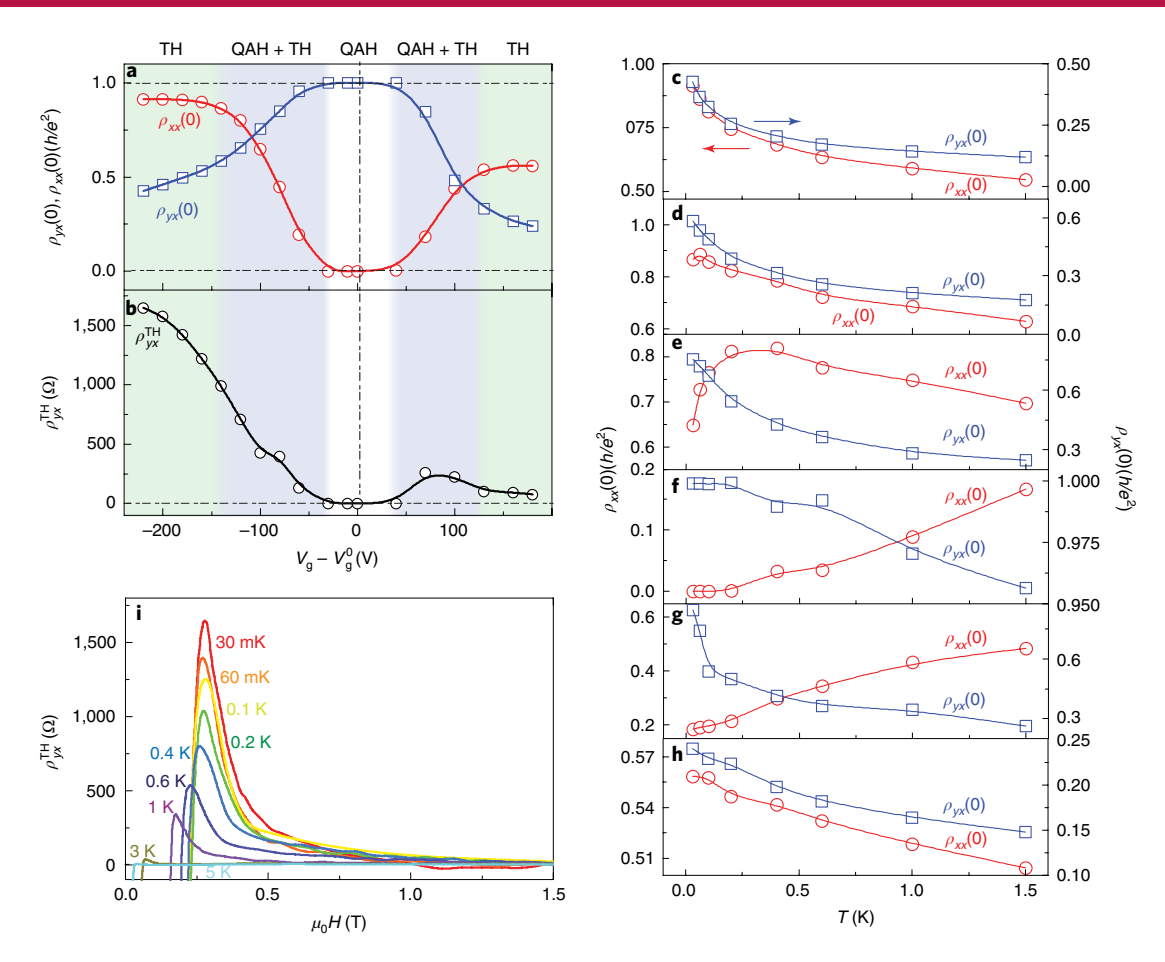


Fig. 3 | Concurrence of the QAH and TH effects in TI sandwich heterostructures. a, Gate dependence of the Hall resistance $\rho_{yx}(0)$ (empty blue squares) and the longitudinal resistance $\rho_{xx}(0)$ (empty red circles) at zero magnetic field and T = 30 mK. **b**, Gate dependence of the TH resistance ρ_{yx}^{TH} at T = 30 mK. The regions of concurrence of the QAH and TH effects are shaded light blue. **c-h**, Temperature dependence of the Hall resistance $\rho_{yx}(0)$ (empty blue squares) and the longitudinal resistance $\rho_{xx}(0)$ (empty red circles) for different gates ($V_g - V_g^0$) of -220 V (**c**), -140 V (**d**), -100 V (**e**), 0 V (**f**), +70 V (**g**) and +180 V (**h**). **i**, $\mu_0 H$ dependence of ρ_{yx}^{TH} for different T at $V_g = V_g^{TH,max}$. ρ_{yx}^{TH} decreases with increasing temperature. ρ_{yx}^{TH} is 1.65 KΩ at T = 30 mK and disappears at T = 5 K. The uncertainty of the data shown in **a-h** is reflected by the size of the symbols. The primary source of the uncertainty is the hysteretic charging effect of the SrTiO₃ substrate.

feature also monotonically decreases with increasing T. We summarize the peak value of $\rho_{yx}^{\rm TH}$ (that is, $\rho_{yx}^{\rm TH,max}$) as a function of $V_{\rm g}-V_{\rm g}^0$) at different temperatures. The $\rho_{yx}^{\rm TH}$ curve at each T is asymmetric between $V_{\rm g} < V_{\rm g}^0$ and $V_{\rm g} > V_{\rm g}^0$. When $60~{\rm mK} \le T \le 1~{\rm K}$, the $\rho_{yx}^{\rm TH}$ shows a peak when $V_{\rm g} < V_{\rm g}^0$ (Supplementary Fig. 7g). This observation indicates that the DM interaction strength is maximized when the chemical potential crosses the bulk valence bands.

Calculations of spin susceptibility and DM interaction

To understand the experimental observations, we propose a model based on the emergence of chiral spin textures around the $\mu_0 H_c$ regime. The observed hump structure in ρ_{yx} has been observed in a variety of non-collinear magnetic systems, particularly skyrmion systems ¹⁴⁻¹⁷, and is regarded as the key signature for the chirality of skyrmions. However, our sample has a robust FM ground state for the occurrence of the QAH effect at low $\mu_0 H$, and thus stable skyrmions are unlikely to be formed ³⁴. Our theoretical calculation (Supplementary Fig. 17 and the relevant discussion) confirms that the magnetic TI sample is dominated by FM states (that is, Heisenberg magnetic coupling). As the TH effect only occurs near the $\mu_0 H_c$ regime, this fact motivated us to consider the possible chiral spin textures during magnetization reversal. During a FM transition, magnetic domains with opposite polarization are nucleated. The presence of a strong DM interaction gives rises to

chiral walls at domain boundaries (Fig. 4a,b). The net scalar chirality $Q = \sum S_1(S_2 \times S_3)$ is thus non-zero and leads to the TH effect, in which S_1 , S_2 and S_3 are three neighbouring spins. This is similar to the emergent chirality reported in the literature^{35–37}, in which magnetization reversal is driven by thermal fluctuations. The DM interaction is essential because chirality is caused by the canting of neighbouring spins. Furthermore, as the scalar chirality Q respects full rotational symmetry, whereas the DM interaction strength D breaks inversion symmetry, $Q \approx D^2$. The TH effect observed in our experiment can thus be understood qualitatively by investigating the DM interaction in magnetic TI samples.

The DM interaction is attributed to the strong spin-orbit coupling in our system. It can be computed via the spin susceptibility of a simplified model for TI films³⁸. The Hamiltonian consists of two parts: the SS Hamiltonian $H_{\rm ss}$, and the bulk state Hamiltonian $H_{\rm QW}$ which describes the quantum well (QW) states due to the quantum confinement effect (Supplementary Section VI). The energy dispersions of the SS and QW bands are shown in Fig. 4c. For simplicity, only one set of QW bands are included, but the inclusion of more QW bands is straightforward and does not affect the qualitative physical picture. The Dirac cones of SS bands are close to the valence band top, which is consistent with the early theoretical and experimental studies^{32,33,39}. Electrons couple to the magnetization M via $H_{\rm Zeeman} = -M\Gamma$, where Γ are proper 4×4 matrices

ARTICLES NATURE MATERIALS

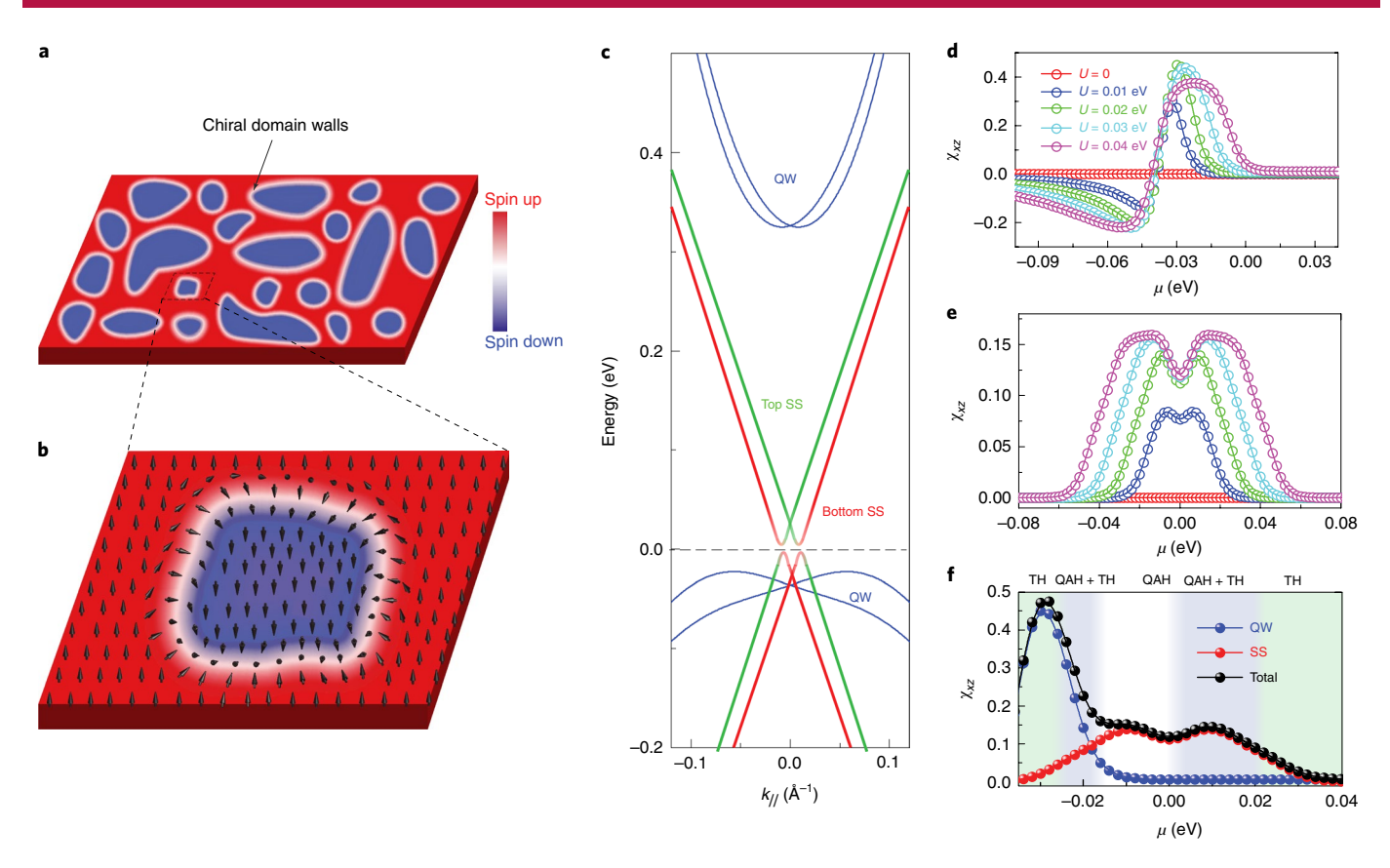


Fig. 4 | **Chiral domain walls and theoretical interpretations of the appearance of the TH effect. a**, The formation of the chiral domain walls during magnetization reversals. **b**, A magnified view that depicts the spin distribution of the chiral domain wall. **c**, The energy dispersions of the SSs and bulk QW bands in magnetic TI. **d**, **e**, χ_{xz} as a function of chemical potential μ for the QW (**d**) and SS (**e**) under different asymmetric potentials *U*. **f**, The QW contribution to χ_{xz} SS contribution to χ_{xz} and the total χ_{xz} in the magnetic TI sandwich heterostructures when U = 0.02 eV, $q_x = 0.005$ Å⁻¹ and $q_y = 0$ in **d-f**.

for electron spin operators. The spin susceptibility $\chi_{\alpha\beta}(\alpha,\beta=x,y,z)$ is evaluated for the model Hamiltonian based on linear response theory $\chi_{\alpha\beta}(q) = \frac{T}{2V} \text{Tr} [G_0(q+k, i\omega_m) \Gamma_\alpha G_0(k, i\omega_m) \Gamma_\beta]$, where ω_m is frequency. DM interaction is given by $D_{\alpha}(q) = \varepsilon_{\alpha\beta\gamma}\chi_{\beta\gamma}(q)$ where ε is the Levi-Civita symbol. As the system breaks mirror symmetry with respect to the xy plane, χ_{xy} = 0, and we thus focus on the off-diagonal components χ_{xz} and χ_{yz} . As expected from the Moriya rule⁴⁰, χ_{xz} (χ_{yz}) is linearly proportional to the momentum $q_x(q_y)$ (Supplementary Fig. 18). By choosing a non-zero q_x value, we calculated χ_{xz} as a function of energy for the QW states and SSs with different asymmetric potential U (Fig. 4d,e) and found a non-zero U is, indeed, required to break the inversion symmetry and induce a finite χ_{xx} . Note that in real samples, in addition to the chemical potential (μ) , U also depends on V_g , but, as discussed in Supplementary Information, its dependence on $V_{\rm g}$ is much weaker in our experiment. The SSs contribution to χ_{xz} shows a double peak structure around the charge neutral point. For the bulk QW states, χ_{xz} reveals a peak when μ lies between two spin-split (valence) bands and then drops and even changes its sign when μ crosses both spin bands. The bulk conduction band is well above the energy range of interest (-30-+40 meV) and thus does not contribute. Figure 4f shows the total χ_{xz} , which behaves similarly to ρ_{yx}^{TH} in our experiment (Fig. 3b). The large asymmetry between the electron- and hole-doping sides arises because the SS is close to the valence band. but well below the conduction band. At $V_{\rm g} < V_{\rm g}^0$, a large contribution to χ_{xz} from the bulk valence-band top significantly enhances the DM interaction and ho_{yx}^{TH} in consequence. We note that including more bulk QW states in the model can further enhance the DM interaction in the holedoping regime. However, the SS contribution prevails in the $V_{\rm g} > V_{\rm o}^0$

regime. When μ is well above the charge neutral point, χ_{xz} vanishes, which is consistent with $\rho_{yx}^{\rm TH}$ in the electron doping regime.

Discussion and conclusion

We note that χ_{xz} is non-zero near the charge neutral point, but in our experiment ρ_{yx}^{TH} is not seen, particularly at low temperatures. This is because in the perfect QAH regime there are no bulk carriers to probe the chiral spin textures. This scenario is validated through numerical simulation of the TH effect for a single chiral domain wall (Supplementary Section VII). At higher temperatures (0.4 K to ~3 K), bulk carriers can be thermally excited and ρ_{yx}^{TH} gradually decreases (Fig. 3i and Supplementary Fig. 7g). At even higher temperatures (>5 K), the vanishing of ρ_{yx}^{TH} is because the thermal fluctuation is larger than the energy scale of the DM interaction and thus destroys the chirality of the magnetic domain walls.

A recent experiment suggests an alternative interpretation of the hump feature of ρ_{yx} observed in the SrIrO₃/SrRuO₃/SrTiO₃ sandwich structures⁴¹. Here, the SrIrO₃/SrRuO₃ and SrRuO₃/SrTiO₃ interfaces have opposite signs of the AH contribution and different μ_0H_c values. In this sandwich sample, the antiferromagnetic alignment configuration between the two magnetic interfaces induces a larger ρ_{yx} than the FM alignment. This can lead to the TH effect-like hump structure. However, this scenario is unlikely to occur in our samples for several reasons. First, ρ_{yx} with a negative sign together with a significantly enhanced μ_0H_c has not been observed in Cr-doped (Bi,Sb)₂Te₃ samples. Second, as a control experiment, we grew 5QL V-doped TI (Bi,Sb)₂Te₃ on top of the 3-5-3 sandwich sample and used the exchange coupling to increase the μ_0H_c of the top Cr-doped TI layer. This structure configuration favours the formation of the

NATURE MATERIALS ARTICLES

antiferromagnetic alignment between the top and bottom Cr-doped TI layers. The hump feature in this control sample, however, disappears rather than being enhanced (Supplementary Fig. 16). Finally, our magnetization measurements show no additional step near $\mu_0 H_c$ in our samples (Supplementary Fig. 3).

To summarize, we fabricated magnetic TI sandwich heterostructures and observed the concurrence of the QAH and TH effects by applying an electrostatic gating voltage. This concurrence indicates an interplay between the chiral edge states and the chiral spin textures in magnetic TI heterostructures that deserves further experimental and theoretical studies. The chiral spin texture associated with the TH effect can be utilized to record the spin information³⁴, and this spin information can be transferred through the chiral edge channels of the QAH effect. The marriage of the chiral edge states and chiral spin textures potentially opens the door for further explorations of proof-of-concept magnetic TI-based spintronic and electronic devices.

Online content

Any methods, additional references, Nature Research reporting summaries, source data, extended data, supplementary information, acknowledgements, peer review information; details of author contributions and competing interests; and statements of data and code availability are available at https://doi.org/10.1038/s41563-020-0605-z.

Received: 28 January 2019; Accepted: 3 January 2020; Published online: 3 February 2020

References

- Hasan, M. Z. & Kane, C. L. Colloquium: topological insulators. Rev. Mod. Phys. 82, 3045–3067 (2010).
- Qi, X. L. & Zhang, S. C. Topological insulators and superconductors. Rev. Mod. Phys. 83, 1057–1110 (2011).
- Nagaosa, N. & Tokura, Y. Topological properties and dynamics of magnetic skyrmions. Nat. Nanotechnol. 8, 899–911 (2013).
- Nagaosa, N., Sinova, J., Onoda, S., MacDonald, A. H. & Ong, N. P. Anomalous Hall effect. Rev. Mod. Phys. 82, 1539–1592 (2010).
- Haldane, F. D. M. Model for a Quantum Hall effect without Landau levels: condensed-matter realization of the 'parity anomaly'. *Phys. Rev. Lett.* 61, 2015–2018 (1988).
- Liu, C. X., Qi, X. L., Dai, X., Fang, Z. & Zhang, S. C. Quantum anomalous Hall effect in Hg_{1-y}Mn_yTe quantum wells. *Phys. Rev. Lett.* 101, 146802 (2008).
- Qi, X. L., Hughes, T. L. & Zhang, S. C. Topological field theory of timereversal invariant insulators. *Phys. Rev. B* 78, 195424 (2008).
- 8. Yu, R. et al. Quantized anomalous Hall effect in magnetic topological insulators. *Science* **329**, 61–64 (2010).
- Chang, C. Z. et al. Experimental observation of the quantum anomalous hall effect in a magnetic topological insulator. Science 340, 167–170 (2013).
- Chang, C. Z. et al. High-precision realization of robust quantum anomalous Hall state in a hard ferromagnetic topological insulator. *Nat. Mater.* 14, 473–477 (2015)
- Checkelsky, J. G. et al. Trajectory of the anomalous Hall effect towards the quantized state in a ferromagnetic topological insulator. *Nat. Phys.* 10, 731–736 (2014).
- Kou, X. F. et al. Scale-invariant quantum anomalous Hall effect in magnetic topological insulators beyond the two-dimensional limit. *Phys. Rev. Lett.* 113, 137201 (2014).
- Mogi, M. et al. Magnetic modulation doping in topological insulators toward higher-temperature quantum anomalous Hall effect. *Appl. Phys. Lett.* 107, 182401 (2015).

- Neubauer, A. et al. Topological Hall effect in the A phase of MnSi. Phys. Rev. Lett. 102, 186602 (2009).
- Lee, M., Kang, W., Onose, Y., Tokura, Y. & Ong, N. P. Unusual Hall effect anomaly in MnSi under pressure. *Phys. Rev. Lett.* 102, 186601 (2009).
- Kanazawa, N. et al. Large topological Hall effect in a short-period helimagnet MnGe. Phys. Rev. Lett. 106, 156603 (2011).
- 17. Huang, S. X. & Chien, C. L. Extended skyrmion phase in epitaxial FeGe(111) thin films. *Phys. Rev. Lett.* **108**, 267201 (2012).
- Matsuno, J. et al. Interface-driven topological Hall effect in SrRuO₃-SrIrO₃ bilayer. Sci. Adv. 2, e1600304 (2016).
- Ohuchi, Y. et al. Electric-field control of anomalous and topological Hall effects in oxide bilayer thin films. Nat. Commun. 9, 213 (2018).
- Yasuda, K. et al. Geometric Hall effects in topological insulator heterostructures. Nat. Phys. 12, 555–559 (2016).
- Liu, C. et al. Dimensional crossover-induced topological Hall effect in a magnetic topological insulator. Phys. Rev. Lett. 119, 176809 (2017).
- Chen, Y. L. et al. Experimental realization of a three-dimensional topological insulator, Bi₁Te₂. Science 325, 178–181 (2009).
- Zhang, J. S. et al. Band structure engineering in (Bi_{1-x}Sb_x)₂Te₃ ternary topological insulators. Nat. Commun. 2, 574 (2011).
- Zhu, J. J., Yao, D. X., Zhang, S. C. & Chang, K. Electrically controllable surface magnetism on the surface of topological insulators. *Phys. Rev. Lett.* 106, 097201 (2011).
- Ye, F., Ding, G. H., Zhai, H. & Su, Z. B. Spin helix of magnetic impurities in two-dimensional helical metal. *Eur. Phys. Lett.* 90, 47001 (2010).
- Xiao, D. et al. Realization of the axion insulator state in quantum anomalous Hall sandwich heterostructures. *Phys. Rev. Lett.* 120, 056801 (2018).
- 27. Mogi, M. et al. A magnetic heterostructure of topological insulators as a candidate for an axion insulator. *Nat. Mater.* **16**, 516–521 (2017).
- Mogi, M. et al. Tailoring tricolor structure of magnetic topological insulator for robust axion insulator. Sci. Adv. 3, eaao1669 (2017).
- 29. Zhang, Y. et al. Crossover of the three-dimensional topological insulator Bi₂Se₃ to the two-dimensional limit. *Nat. Phys.* **6**, 584–588 (2010).
- Chang, C. Z. et al. Thin films of magnetically doped topological insulator with carrier-independent long-range ferromagnetic order. Adv. Mater. 25, 1065–1070 (2013).
- Zhang, Z. C. et al. Electrically tuned magnetic order and magnetoresistance in a topological insulator. *Nat. Commun.* 5, 4915 (2014).
- Chang, C. Z. et al. Zero-field dissipationless chiral edge transport and the nature of dissipation in the quantum anomalous Hall state. *Phys. Rev. Lett.* 115, 057206 (2015).
- 33. Wang, W. B. et al. Direct evidence of ferromagnetism in a quantum anomalous Hall system. *Nat. Phys.* **14**, 791–795 (2018).
- Jiang, W. J. et al. Skyrmions in magnetic multilayers. Phys. Rep. 704, 1–49 (2017).
- Hou, W. T., Yu, J. X., Daly, M. & Zang, J. D. Thermally driven topology in chiral magnets. *Phys. Rev. B* 96, 140403(R) (2017).
- 36. Bottcher, M., Heinze, S., Egorov, S., Sinova, J. & Dupe, B. *B–T* phase diagram of Pd/Fe/Ir(111) computed with parallel tempering Monte Carlo. *N. J. Phys.* **20**, 103014 (2018).
- Wang, W. B. et al. Spin chirality fluctuation in two-dimensional ferromagnets with perpendicular magnetic anisotropy. *Nat. Mater.* 18, 1054–1059 (2019).
- Liu, C. X. et al. Oscillatory crossover from two-dimensional to threedimensional topological insulators. Phys. Rev. B 81, 041307 (2010).
- Li, W. et al. Origin of the low critical observing temperature of the quantum anomalous Hall effect in V-doped (Bi,Sb)₂Te₃ film. Sci. Rep. 6, 32732 (2016).
- Moriya, T. Anisotropic superexchange interaction and weak ferromagnetism. Phys. Rev. 120, 91–98 (1960).
- 41. Groenendijk D. J. et al. Berry phase engineering at oxide interfaces. Preprint at http://arXiv/abs/1810.05619 (2018).

Publisher's note Springer Nature remains neutral with regard to jurisdictional claims in published maps and institutional affiliations.

© The Author(s), under exclusive licence to Springer Nature Limited 2020

ARTICLES NATURE MATERIALS

Methods

Molecular beam epitaxy growth of TI sandwich heterostructure. The magnetic TI sandwich heterostructure growth was carried out using a Veeco/Applied EPI molecular beam epitaxy system with a vacuum of $\sim\!2\times10^{-10}$ mbar. The heattreated insulating SrTiO $_3(111)$ substrates were outgassed at $\sim\!53\,^{\circ}\mathrm{C}$ for 1 h before the growth of the TI sandwich heterostructures. High-purity Bi (5 N), Sb (6 N), Cr (5 N) and Te (6 N) were evaporated from Knudsen effusion cells. During growth of the TI, the substrate was maintained at $\sim\!240\,^{\circ}\mathrm{C}$. The flux ratio of Te per (Bi+Sb) was set to be >10 to prevent Te deficiency in the samples. The magnetic or non-magnetic TI growth rate was at $\sim\!0.25\,\mathrm{QL\,min^{-1}}$. Each layer of the sandwich heterostructure was grown with different Bi/Sb ratios by adjusting their Knudsencell temperatures to tune the chemical potential close to its charge neutral point. Finally, to avoid possible contamination, a 10 nm thick Te layer was deposited at room temperature on top of the sandwich heterostructures prior to their removal from the molecular beam epitaxy chamber for ex situ transport and other characterization measurements.

Hall-bar device fabrications. The magnetic TI sandwich heterostructures grown on $2\,\text{mm}\times10\,\text{mm}$ heat-treated insulating $SrTiO_3(111)$ were scratched into a Hall bar geometry using a computer-controlled probe station. The effective area of the Hall bar device was ~1 mm $\times0.5$ mm. The electrical ohmic contacts for the transport measurements were made by pressing indium spheres on the Hall bar. The bottom gate electrode was prepared through an indium foil on the back side of the $SrTiO_3$ substrate.

Transport measurements. Transport measurements were conducted using both a Quantum Design Physical Property Measurement System (PPMS; $2\,K,9\,T$) and a Leiden Cryogenics dilution refrigerator ($10\,mK,9\,T$) with the magnetic field applied perpendicular to the film plane. The bottom gate voltage was applied using a Keithley 6430. The excitation currents in the d.c. PPMS measurements ($\geq 2\,K$) was $1\,\mu A$. We used a PicoWatt AVS-47 a.c. resistance bridge to conduct the dilution refrigerator measurements ($< 2\,K$) with a low excitation current ($1\,nA$) to suppress the heating effect. The results reported here were reproduced on two samples measured in the dilution refrigerator and more than ten samples measured in the PPMS. All the transport results shown here were anti-symmetrized as a function of the magnetic field. More transport results are given in the Supplementary Information.

Theoretical calculations. The QW Hamiltonian is

 $H_{\mathrm{QW}} = \varepsilon_0(k) + N(k)\tau_z + A\left(k_y\sigma_x - k_x\sigma_y\right)\tau_x + U\tau_x$, where Pauli matrices σ stand for spins and τ stand for two orbitals, and $\varepsilon = C_0 + C_1k^2$ and $N = N_0 + N_2k^2$. Here C_0 , C_1 , N_0 and N_1 are material dependent parameters. Different sets of QW states differ by different C_0 and N_0 values. The dispersion in Fig. 4c takes values of $C_0 = 0.145$ eV, $C_2 = 10.0$ eV Å 2 , $N_0 = -0.18$ eV, $N_2 = 15.0$ eV Å 2 , A = 3.0 eV Å and U = 0.02 eV. Coupling of the QW electrons to magnetization M is simply $H_{Zeeman}^{\mathrm{QW}} = -M\sigma$. However, the SSs have the Hamiltonian $H_{\mathrm{SS}} = v_{\mathrm{F}}\left(k_y\sigma_x - k_x\sigma_y\right)\tau_z + U\tau_z + m_0\sigma_x$, where v_{F} is Fermi velocity, m_0 is the mass of electron, σ stands for spins, but τ stands for two surfaces instead. U is the asymmetric potential applied to two

surfaces. The coupling to magnetizations $M^{\rm t}$ and $M^{\rm b}$ on the top and bottom surfaces, respectively, is $H_{\rm Zeeman}^{\rm SS}=M^{\rm t}\sigma(1+\tau_z)/2+M^{\rm b}\sigma(1-\tau_z)/2$. In Fig. 4c, we use $m_0=0.005\,{\rm eV},\, \nu_{\rm F}=3.0\,{\rm eV}$ Å and $U=0.02\,{\rm eV}$.

Data availability

The data that support the findings of this study are available from C.-Z.C. on reasonable request.

Code availability

The code for theoretical calculations of spin susceptibility and DM interaction and simulations of the quantum transport simulation through a single chiral magnetic domain wall from C.L. and J.Zang on reasonable request.

Acknowledgements

The authors thank X. D. Xu, B. H. Yan, H. Z. Lu and W. D. Wu for helpful discussions. D.X. and N.S. acknowledge support from an ONR grant (N-000141512370) and Penn State 2DCC-MIP under NSF grant DMR-1539916. J.-H.S. and M.H.W.C. acknowledge the support from NSF grant DMR-1707340. C.L. acknowledges the support from an ONR grant (N00014-15-1-2675 and renewal No. N00014-18-1-2793). D.A. and J.Zang acknowledge the support from DOE grants (DE-SC0016424 and DE-SC0020221). C.-Z.C. acknowledges the support from the Gordon and Betty Moore Foundation's EPiQS Initiative (Grant GBMF9063) and an ARO Young Investigator Program Award (W911NF1810198). Support for transport measurements and data analysis was provided by DOE grant (DE-SC0019064).

Author contributions

N.S., M.H.W.C. and C.-Z.C. conceived and designed the experiment. D.X. grew the sandwich heterostructure samples with the help of N.S. and C.-Z.C. F.W., K.W. and J.J. performed characterizations of the samples with the help of C.-Z.C. J.J., F.W., J.-H.S., R.X. and M.K. performed the dilution refrigerator measurements with the help of M.H.W.C. and C.-Z.C. J.J., F.W., Y.-F.Z. and L.Z. carried out the PPMS transport measurement with the help M.H.W.C. and C.-Z.C. D.A., J.Zhang, J. Zang and C. L. provided theoretical support and did all the theoretical calculations. J.J., J.Zang, C.L., N.S., M.H.W.C. and C.-Z.C. analysed the data and wrote the manuscript with contributions from all authors.

Competing interests

The authors declare no competing interests.

Additional information

Supplementary information is available for this paper at https://doi.org/10.1038/s41563-020-0605-z.

 $\label{lem:correspondence} \textbf{Correspondence and requests for materials} \ \text{should be addressed to N.S., M.H.W.C.} \ \text{or C.-Z.C.}$

Reprints and permissions information is available at www.nature.com/reprints.